FRONTIERS OF PHYSICS

RESEARCH ARTICLE
Volume 17 / Issue 5 / 53509 / 2022

High performance of hot-carrier generation, transport and injection in TiN/TiO_2 junction

Tingting Liu[1,2,*], Qianjun Wang[3,*], Cheng Zhang[1,2], Xiaofeng Li[1,2,†], Jun Hu[3,4,‡]

1 School of Optoelectronic Science and Engineering & Collaborative Innovation Center of Suzhou Nano Science and Technology, Soochow University, Suzhou 215006, China
2 Key Lab of Advanced Optical Manufacturing Technologies of Jiangsu Province & Key Lab of Modern Optical Technologies of Education Ministry of China, Soochow University, Suzhou 215006, China
3 School of Physical Science and Technology, Soochow University, Suzhou 215006, China
4 School of Physical Science and Technology, Ningbo University, Ningbo 315211, China
Corresponding authors. E-mail: †xfli@suda.edu.cn, ‡hujun2@nbu.edu.cn
*These authors contributed equally to this work.
Received March 1, 2022; accepted April 17, 2022

ABSTRACT

Improving the performance of generation, transport and injection of hot carriers within metal/semiconductor junctions is critical for promoting the hot-carrier applications. However, the conversion efficiency of hot carriers in the commonly used noble metals (e.g., Au) is extremely low. Herein, through a systematic study by first-principles calculation and Monte Carlo simulation, we show that TiN might be a promising plasmonic material for high-efficiency hot-carrier applications. Compared with Au, TiN shows obvious advantages in the generation (high density of low-energy hot electrons) and transport (long lifetime and mean free path) of hot carriers. We further performed a device-oriented study, which reveals that high hot-carrier injection efficiency can be achieved in core/shell cylindrical TiN/TiO_2 junctions. Our findings provide a deep insight into the intrinsic processes of hot-carrier generation, transport and injection, which is helpful for the development of hot-carrier devices and applications.

Keywords metal/semiconductor junction, plasmonic material, hot-carrier generation, lifetime and mean free path, injection efficiency

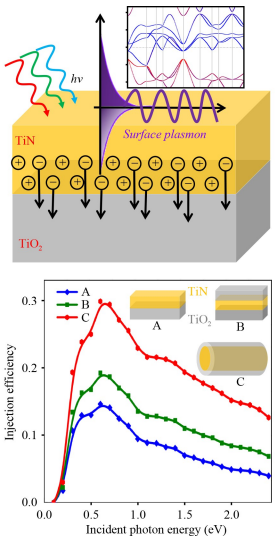

1 Introduction

Surface plasmons in a metal/semiconductor (M/S) junction excited by light irradiation have sparked great interest in the communities of condensed matter physics and materials science recently, because of the promising applications for solar energy harvest, photoelectric detection and photocatalysis [1–3]. For an M/S junction, non-radiative decay of surface plasmons in the metal likely generates hot carriers that could be injected into the adjacent semiconductor by surmounting the Schottky barrier at the M/S interface [4]. Considering the height of Schottky barrier of M/S junction is often below the band gap of the corresponding semiconductor, the photon energy requisite to obtain free carriers in the semiconductor of an M/S junction through the hot-carrier injection could be lower than that of direct interband transitions from valence bands to conduction bands. The noble metals especially Au are most widely used in plasmonic hot-carrier devices, due to their excellent environmental stability, good electrical conductivity, high plasmon enhanced hot-carrier generation rate, and long lifetime

https://doi.org/10.1007/s11467-022-1171-4

and mean free path of hot carriers [5–8]. However, Au is not a sufficiently ideal plasmonic metal for practical hot-carrier devices. First, it is an expensive and scarce resource on the earth. Second, the density of the light-excited hot carriers near the Fermi level is very low, because of the specific electronic structures of Au. Third, the work function (~5.1 eV) of Au is high, which usually results in large Schottky barrier and hence makes the hot-carrier injection efficiency of Au-based hot-carrier devices fundamentally inefficient [7]. Some groups have theoretically and experimentally investigated alternative non-noble metals for hot-carrier devices, such as Al, Cu, and Ag [9]. Nevertheless, exploring better plasmonic materials is still of high importance and interest for the development of hot-carrier devices.

Revealing the underlying physical mechanisms of the generation, transport and injection properties of hot carriers in M/S junctions is the prerequisite for designing hot-carrier devices [10–12]. These properties are closely associated with the electronic structures of both metal and semiconductor. The decay of plasmons lifts electrons from occupied states to unoccupied states through inter-band and intraband transitions. Hence, the energy distribution of hot carriers is determined by the band structure of the metal and the photon energy of the incident light [13, 14]. The transport property is strongly related to the lifetimes and mean free paths of hot carriers, so it is significantly affected by the scatterings from electrons, phonons, defects and impurities. Generally, the negative influence of defects and impurities might be relieved by controlling the quality of M/S junctions, thus they are not the crucial factors for the transport of hot carriers [15]. However, electron–electron scattering (EES) and electron–phonon scattering (EPS) are inevitable, and they play important roles in the transport procedure. The hot-carrier injection efficiency is determined by the Schottky barrier at the M/S interface which stems from the band alignment between the metal and semiconductor [15, 16]. Clearly, revealing the corresponding underlying physical mechanisms rely on accurate calculations of the electronic properties especially the EES and EPS. However, these calculations are still difficult and the systematic research on the whole process of the generation, transport and injection of hot carriers in M/S junctions is still lacking [7, 13, 14].

In this paper, we provide a standard procedure to theoretically explore the generation, transport and injection performances of hot carriers in plasmonic material-based M/S junctions. We chose TiO_2 as the semiconductor layer, because it possesses good electronic properties and has been widely used in hot-carrier devices [17–20]. For the plasmonic material, the family of the transition metal nitrides may be good candidates to replace the noble metals [21–26]. In particular, TiN has drawn extensive attention in recent years, because it exhibits excellent capability in photoelectric conversion and detection [27–29]. Especially, it is cheap compared to the noble metals. The generation, transport and injection of hot carriers in the Au/TiO_2 and TiN/TiO_2 junctions were investigated through first-principles calculations and Monte Carlo simulations [30–32]. We found that TiN is indeed a better plasmonic material than Au. TiN possesses higher concentration of low-energy hot carriers than Au, and the lifetime and mean free path of the hot carriers are comparable to those in Au. Large hot-carrier injection efficiency can be achieved in the core/shell cylindrical TiN/TiO_2 junction. Accordingly, the TiN/TiO_2 junction might be promising for practical hot-carrier applications.

2 Calculation methods

We used the Vienna *ab initio* Simulation Package (VASP) [33, 34] in the framework of the density functional theory (DFT) to calculate the atomic structures and electronic properties. The electron–ion interactions were described with the projector augmented wave (PAW) approach [35]. The exchange-correlation potential was considered at the level of the generalized gradient approximation (GGA) with Perdew–Burke–Ernzerhof (PBE) functional for TiN, and Perdew–Burke–Ernzerhof revised for solids (PBEsol) [36] functional for Au. According previous report, the spin–orbit coupling (SOC) and a rotationally invariant DFT+U correction [37] with $U = 2.4$ eV is necessary for Au [13, 14]. A kinetic energy cutoff was set to 500 eV and a 10 × 10 × 10 Monkhorst–Pack mesh in the Brillouin Zones was employed. The calculated electronic structures of Au and TiN are consistent with previous calculations and experiments [38, 39]. The crystal structures were fully relaxed until the residual forces on each atom are less than 0.01 eV/Å. The optimized lattice constants of Au and TiN are 4.06 Å and 4.23 Å, respectively, consistent with the corresponding experimental values 4.08 Å [40] and 4.24 Å [41]. The EES and EPS were estimated by using the open-source code JDFTx [42] with full-relativistic norm-conserving pseudopotentials [43]. The plane-wave cutoff and Fermi–Dirac smearing were set to 30 and 0.01 Hartree, respectively. The Brillouin zone was sampled with a 20 × 20 × 20 Monkhorst–Pack mesh. The matrix elements of the electron–phonon coupling were calculated with the maximally-localized Wannier functions [44] in a 2 × 2 × 2 supercell. The k-point mesh for the Wannier function interpolation was adopted as 24 × 24 × 24.

3 Results and discussion

3.1 Electronic properties of bulk Au and TiN

The bulk Au adopts the face-centered cubic (FCC) crystal structure, while TiN crystallizes the rock-salt structure

which is also based on the FCC structure, as shown in Figs. 1(a) and (b). Apparently, each Ti atom locates at the center of the octahedron comprised of the six nearest neighboring N atoms, and vice versa for each N atom. Consequently, the five-fold degenerate Ti-3d orbital splits into two groups: triplet t_{2g} (d_{xy}, d_{xz}, and d_{yz}) and doublet e_g (d_{z^2} and $d_{x^2-y^2}$) orbitals, due to the octahedral crystal field. Then, the t_{2g} and e_g orbitals separately hybridize with the N-2p orbital, forming bonding and antibonding orbitals, as sketched in Fig. 1(d). These hybridized orbitals finally evolve into the energy bands due to the periodic potential in crystal TiN.

The band structure of Au with the path denoted in Fig. 1(c) is displayed in Fig. 2(a). We can see that there are many localized bands in the energy range from −7 eV to −1 eV, while only a few bands cross the Fermi level (E_F). To identify the orbital features of these bands, we plotted the orbital-resolved band structures in Figs. 2(b) and (c). It can be seen that the localized bands bellow E_F are dominated by the Au-5d orbital.

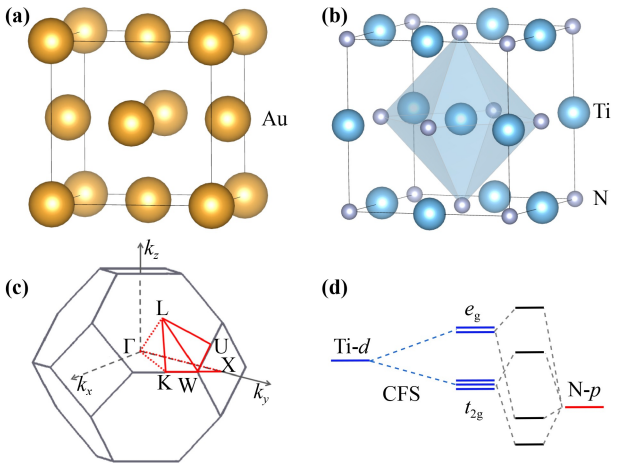

Fig. 1 **(a, b)** Atomic structures of Au and TiN. **(c)** The Brillouin zone. The red lines denote the path for the band structure. **(d)** Schematic energy diagram of the hybridization between the Ti-3d and N-2p orbitals due to the crystal field splitting (CFS) in the octahedron symmetry as indicated in (b).

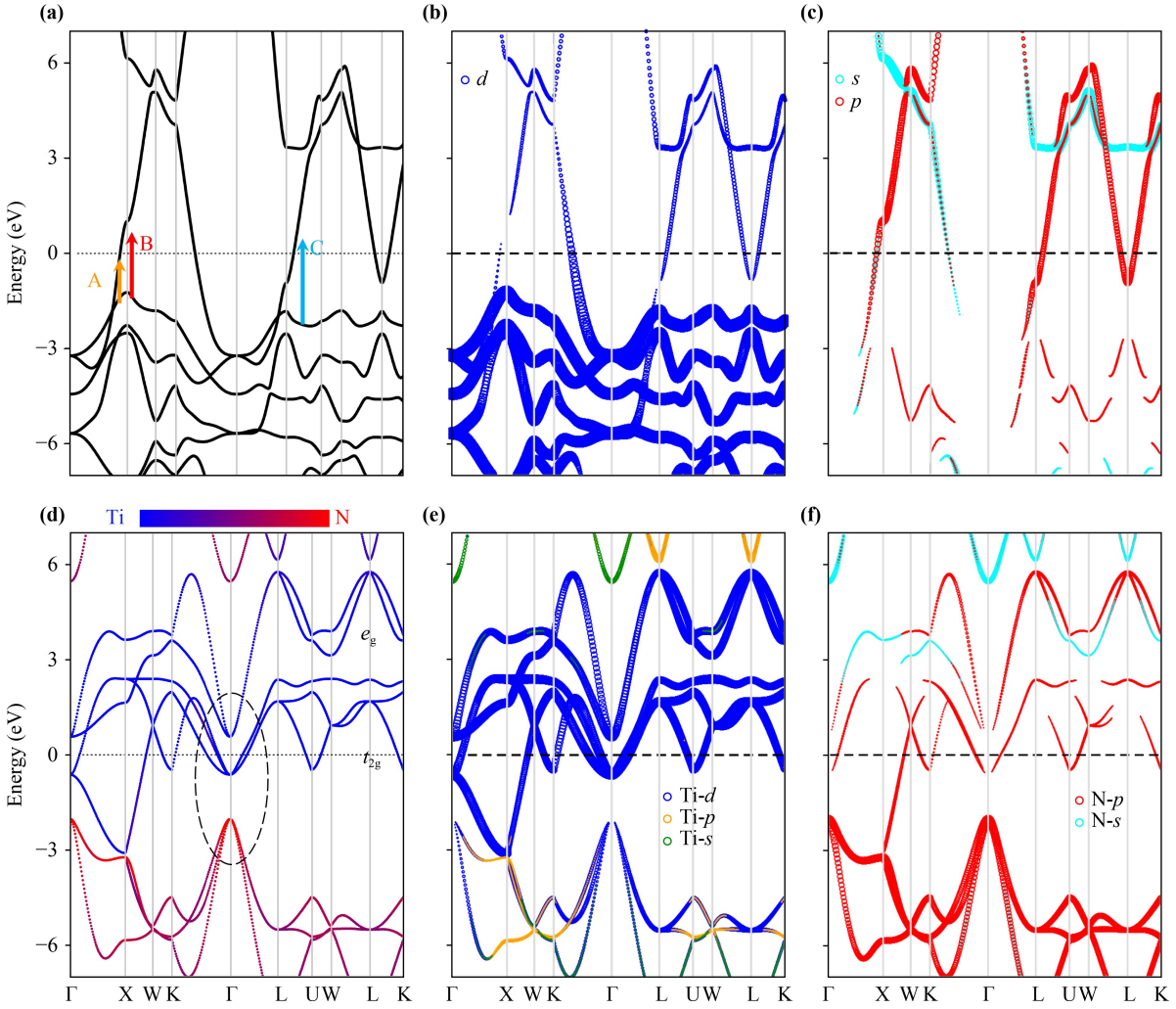

Fig. 2 Band structures of Au (upper panels) and TiN (lower panels). The different colors and sizes of circles in **(b)**, **(c)**, **(e)** and **(f)** indicate the weights of different atomic orbitals. The color bar in **(d)** indicates the weights of Ti and N atoms.

Interestingly, the Au-6p orbital has large contribution to the bands crossing E_F, which originates from the charge transfer between different atomic orbitals due to the crystal field and hybridization between neighboring Au atoms.

Figures 2(d)–(f) show the element- and orbital-resolved band structures of TiN. It can be seen that the bands can be separated into two parts. The upper bands from –1 eV to 6 eV are dominated by the Ti-3d orbital, while the lower bands bellow –2 eV are mainly contributed from the N-2p orbitals. Meanwhile, the energy levels at the Γ point remain completely as atomic orbitals. The three energy levels in the oval in Fig. 2(d) at –2.03 eV, –0.63 eV, and 0.57 eV are the N-2p, Ti-t_{2g}, and Ti-e_g orbitals, respectively. Away from the Γ point, the bands reflect strong hybridization between the orbitals of Ti and N, because of the short Ti–N bond length (2.12 Å). Moreover, the upper bands can be assigned to the antibonding states of the p-t_{2g} and p-e_g hybridizations, compared to the energy diagram in Fig. 1(d). The hybridizations for the lower bands are more complicated, since the N-2p orbital hybridizes with all the orbitals (s, p and d) of Ti.

The band alignment of the metal and semiconductor of an M/S junction, which determines the Schottky barrier at the M/S interface, is important for the transport of hot carriers. We further calculated the band structures of the thin-film models of TiO_2 and TiN, then estimated the work functions of TiO_2 and TiN by taking the energy level of vacuum as reference. The difference of the two work functions corresponds to the the Schottky barrier at the TiN/TiO_2 interface and is only about 0.1 eV, in agreement with previous report [45]. Especially, it is much smaller than that at the Au/TiO_2 interface (~1 eV) [46]. Accordingly, the band gap of TiO_2 covers the energy range from –3.1 eV to 0.1 eV with respect to E_F of TiN, while from –2.1 eV to 1.1 eV for Au.

The total and projected density of states (DOS) of Au and TiN are plotted in Figs. 3(a) and (b). Clearly, the total DOS near E_F in TiN is much larger than that in Au, because there are more bands crossing E_F in TiN than in Au. Therefore, the concentration of low-energy free carriers in TiN is much higher than that in Au, and the free carriers mainly characterize the Ti-3d electrons. Moreover, we can see that the peak of DOS within 0–3 eV features the Ti-t_{2g} orbital, while that within 3–6 eV belongs to the Ti-e_g orbital, according to the energy diagram in Fig. 1(d).

Fermi surface (FS) of metals is another important electronic property which affects the electronic transport in metals. The insets in Figs. 3(a) and (b) display the FSs of Au and TiN, respectively. Clearly, most part of the FS of Au is smooth and far away from the boundary of Brillouin zone. The FS of Au touches the boundary of Brillouin zone within a small region around the "L" point and its equivalents, which contributes to the electron transport. In contrast, the FS of TiN is much more complex compared to that of Au, especially near the boundary of Brillouin zone. Consequently, the anisotropy of electronic transport in TiN is more significant than in Au.

3.2 Hot-carrier generation

The hot-carrier generation rate is proportional to the relative probabilities of the indirect intraband and direct

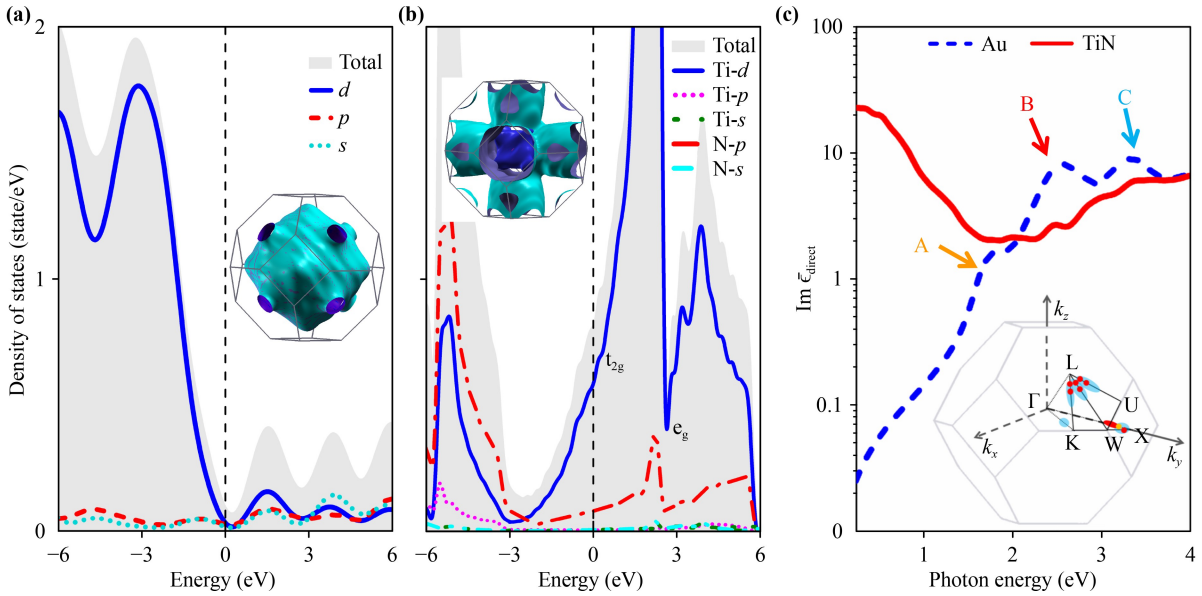

Fig. 3 **(a, b)** Projected densities of states of Au and TiN, respectively. The insets are the corresponding Fermi surfaces. **(c)** Imaginary part of dielectric function for the direct electric dipole transition. The inset highlights the areas where the peaks "A", "B" and "C" mostly originate from.

interband transitions. The indirect transition is associated to the DOS $[\rho(E)]$ and Fermi–Dirac distribution function $[f(E)]$ [47], and the corresponding relative probability of indirect transition is expressed as [48]

$$D(E) = \frac{\rho(E-h\nu)\, f(E-h\nu)\, \rho(E)\, [1-f(E)]}{\int \rho(E-h\nu)\, f(E-h\nu)\, \rho(E)\, [1-f(E)]\, \mathrm{d}E}, \tag{1}$$

where E is the energy of the excited electron and $h\nu$ is the incident photon energy. The direct transition is usually described by the imaginary part of the dielectric function ($\bar{\epsilon}_{\text{direct}}$). Based on the perturbation theory of quantum mechanics for the electric dipole transition, the imaginary part of $\bar{\epsilon}_{\text{direct}}$ can be calculated with the following expression [14]:

$$\begin{aligned}&\lambda^* \cdot \mathrm{Im}\bar{\epsilon}_{\text{direct}}(\omega) \cdot \lambda \\ &= \frac{4\pi^2 e^2}{m_e^2 \omega^2} \int_{\mathrm{BZ}} \frac{\mathrm{d}\boldsymbol{k}}{2\pi^3} \sum_{n'n} (f_{kn} - f_{\boldsymbol{k}n'})\, \delta(\varepsilon_{\boldsymbol{k}n'} - \varepsilon_{kn} \\ &\quad -\hbar\omega) \left| \lambda \cdot \langle \boldsymbol{P} \rangle^{k}_{n'n} \right|^2, \end{aligned} \tag{2}$$

where λ and ω are the polarization vector and angular frequency of incident light, respectively; $\varepsilon_{\boldsymbol{k}n}$ and $f_{\boldsymbol{k}n}$ are the eigenvalue and electron occupancy of the state with wave vector $\boldsymbol{k}$ and band index n; $\langle \boldsymbol{P} \rangle^{\boldsymbol{k}}_{n'n}$ stands for the matrix element of the momentum operator $\boldsymbol{P}$ which can be calculated via $\boldsymbol{P} \equiv \frac{m_e}{i\hbar}[\boldsymbol{r}, \boldsymbol{H}]$. We used the WANNIER90 code [44, 49–50] to calculate the maximum local Wannier functions that were then used to calculate the matrix elements of $\boldsymbol{r}$ and $\boldsymbol{H}$. The Brillouin zone for the integration was sampled by randomly selected k points up to 5×10^6. The more details about the calculation of the relative probabilities of the indirect intraband and direct interband transitions can be found in literatures [14, 48].

The curves of $\bar{\epsilon}_{\text{direct}}$ as a function of $h\nu$ for Au and TiN are shown in Fig. 3(c). When $h\nu < 1.5$ eV, $\bar{\epsilon}_{\text{direct}}$ of TiN is much larger than that of Au, while the values of $\bar{\epsilon}_{\text{direct}}$ for the two cases are comparable in the rest energy range. For Au, there are three peaks centered around 1.7, 2.5 and 3.3 eV, as marked by "A", "B" and "C" in Fig. 3(c). The peak "A" corresponds to the threshold of electric dipole transition in Au, in good agreement with the experimental measurement (1.6–1.8 eV) [14]. According to the selection rules of the electric dipole transition, these peaks are generated mainly by the transition from the occupied 5d orbital to unoccupied 6p orbital, as indicated in Fig. 2(a) and highlighted in the inset in Fig. 3(a). For TiN, the electric dipole transitions mainly occur between the Ti-3d and N-2p orbitals. Since the DOS near E_F in TiN is much larger than that in Au, it is expected that higher density of hot carriers could be produced in TiN.

We set a series of $h\nu$ to estimate the relative probabilities of hot-carrier generation at different energies from indirect and direct transitions in Au and TiN, as plotted in Fig. 4. Generally speaking, larger $h\nu$ results in larger energy of hot carriers, as the peaks of relative probabilities shift away from E_F with increasing $h\nu$. For Au, hot holes (bellow E_F) and hot electrons (above E_F) can be excited only through the indirect intraband transition when $h\nu$ is smaller than 1.2 eV [Fig. 4(a)]. This is because the starting point of the first peak of the direct interband transition is around 1.2 eV, as can be seen in Fig. 3(a). Once the incident photon energy is larger than 1.2 eV, both indirect and direct transitions produce hot holes

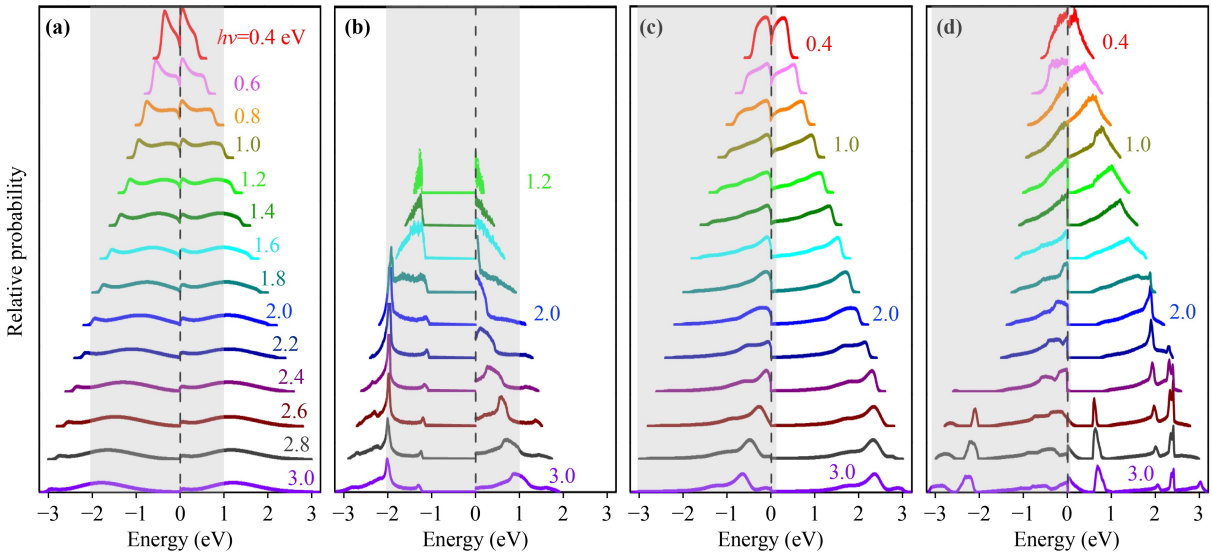

Fig. 4 Relative probability of hot-carrier generation as a function of hot-carrier energy under different incident photon energy $h\nu$. **(a/c)** and **(b/d)** From indirect and direct transitions in Au/Ti, respectively. The Fermi level is set to zero energy. The shadow area denotes the band gap of TiO_2.

and hot electrons. However, the relative probability from the indirect transition is much smaller than that from the direct transition. Furthermore, when $h\nu$ is smaller than 2 eV, the energies of both hot electrons and hot holes except a small part of hot electrons from the indirect transition fall inside the band gap of TiO_2, so the number of effective hot carriers is ignorable. Only when $h\nu$ is larger than 2.6 eV, there is sizable number of effective hot holes with energy centered around –2 eV from the direct transition [Fig. 4(b)]. Clearly, this requirement is disadvantageous for hot-carrier applications which is mostly in the range from the near-infrared light to the low-energy visible light.

Figures 4(c) and (d) present the relative probabilities of hot carriers with different energies from indirect and direct transitions in TiN. Since the band gap of TiO_2 covers the energy range from –3.1 to 0.1 eV, the number of hot holes is insignificant for all considered incident photon energies. On the contrary, almost all hot electrons may turn into effective hot carriers, because their energies fall into the conduction band of TiO_2. In addition, hot carriers can be generated by both indirect and direct transitions even at low-energy incident light, which can be attributed to the large DOS near E_F. The overall relative probabilities from the indirect and direct transitions are comparable with $h\nu$ smaller than 2.0 eV, much different from the feature in Au. When $h\nu$ reaches 2.0 eV, the relative probability from the direct transition exceeds that from the indirect transition, and the energy of hot holes becomes more centralized as indicated by the narrow and sharp peaks in Fig. 4(d). It is possible to identify the contributions of the direct transitions to these peaks, combined with the band structures in Figure 2. For example, when $h\nu$ is 3 eV, the hot electrons with energy around 0.75 eV mainly originate from the transition from the Ti-3d orbital to the N-2p orbital near the Γ point, while the hot electrons with energies of 2, 2.5 and 3eV mainly stem from the transitions around the W, K, Γ points, respectively. On the whole, the generation of hot carriers in TiN is much more efficient than in Au, especially in the near-infrared light and low-energy visible light, which benefits the solar energy harvest with hot-carrier devices.

3.3 Hot-carrier transport and injection

The hot carriers excited in the metal of an M/S junction travel in the metal before they get to the M/S interface, then they might be injected into the semiconductor if their energy is large enough to overcome the Schottky barrier at the M/S interface. The transport process is dominated by the lifetime and mean free path of hot carriers, so it is significantly affected by the EES and EPS [51]. For the sake of practical applications, long lifetime and mean free path are desired. The scattering rates of the EES and EPS are related to the imaginary parts of the corresponding quasiparticle self-energies [14, 15]. The imaginary part of quasiparticle self-energy from the EES can be expressed as [14, 38]

$$\mathrm{Im}\Sigma^{e-e}_{\boldsymbol{k}n} = \int_{\mathrm{BZ}} \frac{\mathrm{d}\boldsymbol{k}'}{(2\pi)^3} \sum_{n'} \sum_{\boldsymbol{G}\boldsymbol{G}'} \widetilde{\rho}_{\boldsymbol{k}'n',\boldsymbol{k}n}(\boldsymbol{G})\, \widetilde{\rho}^{*}_{\boldsymbol{k}'n',kn}(\boldsymbol{G}') \times \frac{4\pi e^2}{|\boldsymbol{k}'-\boldsymbol{k}+\boldsymbol{G}|^2} \mathrm{Im}\left[\epsilon^{-1}_{\boldsymbol{G}\boldsymbol{G}'}(\boldsymbol{k}'-\boldsymbol{k}, \epsilon_{\boldsymbol{k}n}-\epsilon_{\boldsymbol{k}'n'})\right]. \quad (3)$$

Here, $\widetilde{\rho}_{\boldsymbol{k}'n',\boldsymbol{k}n}$ is the plane-wave expansion of the product density $\sum_\sigma u^{\sigma *}_{\boldsymbol{k}'n'}(\boldsymbol{r})\, u^{\sigma}_{\boldsymbol{k}'n'}(\boldsymbol{r})$ of Bloch functions with reciprocal lattice vectors $\boldsymbol{G}$; $\epsilon^{-1}_{\boldsymbol{G}\boldsymbol{G}'}$ is the microscopic dielectric function in a plane-wave basis calculated within the random-phase approximation. For the EPS, the imaginary part of the quasiparticle self-energy can be calculated as [14, 38]

$$\mathrm{Im}\Sigma^{e-ph}_{\boldsymbol{k}n} = \pi \int_{\mathrm{BZ}} \frac{\Omega \mathrm{d}\boldsymbol{k}'}{(2\pi)^3} \sum_{n'\alpha\pm} \left(n_{\boldsymbol{k}'-\boldsymbol{k},\alpha} + \frac{1}{2} \mp \frac{1}{2}\right) \times \delta(\varepsilon_{\boldsymbol{k}'n'} - \varepsilon_{\boldsymbol{k}n} \mp \hbar\omega_{\boldsymbol{k}'-\boldsymbol{k},\alpha}) \left| g^{\boldsymbol{k}'-\boldsymbol{k},\alpha}_{\boldsymbol{k}'n',\boldsymbol{k}n} \right|^2. \quad (4)$$

Here, $\boldsymbol{q} = \boldsymbol{k}' - \boldsymbol{k}$ and $n_{\boldsymbol{q},\alpha}$ are the wave vector and particle number of phonons; $g^{\boldsymbol{k}'-\boldsymbol{k},\alpha}_{\boldsymbol{k}'n',\boldsymbol{k}n}$ is the electron–phonon coupling matrix element with electronic states labeled by electron wave vectors ($\boldsymbol{k}$ and $\boldsymbol{k}'$) and band indices (n and n'); Ω is the volume of unit cell. The total scattering lifetime of hot carriers is $\tau_{\boldsymbol{k}n} = \hbar/(2\mathrm{Im}\Sigma_{\boldsymbol{k}n})$, where $\mathrm{Im}\Sigma_{\boldsymbol{k}n} = \mathrm{Im}\Sigma^{e-e}_{\boldsymbol{k}n} + \mathrm{Im}\Sigma^{e-ph}_{\boldsymbol{k}n}$ [14]. The mean free path is $\lambda_{\boldsymbol{k}n} = \nu_{\boldsymbol{k}n}\tau_{\boldsymbol{k}n}$, where $\nu_{\boldsymbol{k}v} \equiv \frac{\partial \varepsilon_{\boldsymbol{k}n}}{\partial \boldsymbol{k}}$ is the velocity of hot carriers and $\varepsilon_{\boldsymbol{k}n}$ is the eigenvalue of the state with wave vector $\boldsymbol{k}$ and band index n.

The imaginary part of the quasiparticle self-energy from the EES and EPS as well as the corresponding lifetime and mean free path are plotted in Fig. 5. It can be seen that the imaginary part of self-energy of the hot holes in Au is larger than that in TiN, while the situation of the hot electrons is opposite. This is because Au and TiN have larger DOS bellow and above E_F, respectively. In addition, the EES and EPS lead to comparable self-energies for the hot holes in the considered energy range (–5 eV–0), but the former gives rise to significantly larger self-energy for the hot electrons with energy higher than 2 eV. Consequently, the EES and EPS contribute to similar lifetime and mean free path of the hot holes, while for the hot electrons the lifetime and mean free path from the EPS are larger than those from the EES. Particularly, the lifetime and mean free path of the low-energy hot carriers ($|E| \lesssim 1$ eV) from the EES are one- to three-order greater than the others. This is because the imaginary part of self-energy related to this phenomenon is very small, indicating the weak EES in this energy range. In fact, the EES for electrons near E_F is nominally proportional to $(\varepsilon - \varepsilon_f)^2$ due to the phase

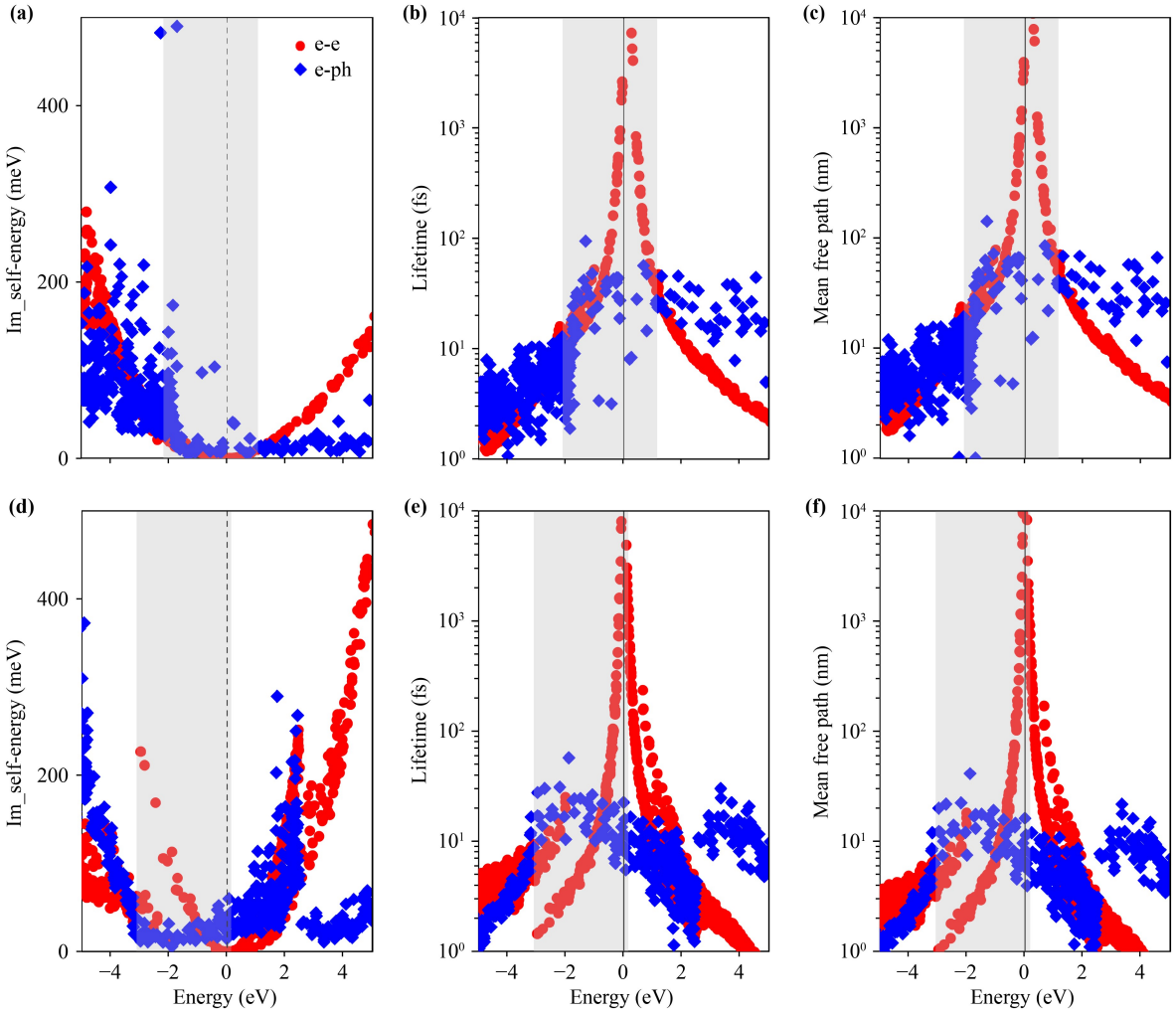

Fig. 5 Imaginary part of quasiparticle self-energy, lifetime and mean free path of hot carriers from electron-electron and electron−phonon scatterings in Au (upper panels) and TiN (lower panels).

space available for scattering [14, 15], so that it is negligible. Nevertheless, this feature does not benefit the transport of hole carriers in Au, since the energies of the effective hot holes and hot electrons in Au are larger than 1 eV due to the band alignment between Au and TiO_2, as shown in Fig. 4. On the contrary, the requirement for the effective hot electrons in TiN is only about 0.1 eV, so the lifetime and mean free path of the low-energy hot electrons are mainly limited by the EPS. Nonetheless, the overall lifetime and mean free path of the effective low-energy hot electrons ($0.1\ \text{eV} < E < 1\ \text{eV}$) in TiN are comparable to the effective low-energy hot electrons in Au ($1\ \text{eV} < E < 2\ \text{eV}$).

Now, we can estimate the injection efficiency (defined as $\eta = N_{inj}/N_{tot}$) of hot carriers by using the Monte Carlo simulation proposed by Blandre *et al.* [32]. N_{tot} is the total number of hot carriers on the metal side (set as 100 000 in this work). N_{inj} is the number of hot carriers that are injected into the semiconductor, so it is associated with the energy distribution of hot carriers, the Schottky barrier at the M/S interface, and the probabilities of the EES and EPS. Unlike the assumption of uniform energy distribution of hot carriers in Ref. [32], we used the calculated energy distribution in Figure 4. Only the hot carriers with energy larger than the Schottky barrier were taken into account. Given that most solar energy is carried by the infrared and visible lights [52, 53], and the energy of the effective hot holes is much larger than that of the effective hot electrons (Fig. 4), we focused on η of the hot electrons with incident photon energy $h\nu$ smaller than 2.5 eV. The initial positions of hot carriers were supposed to be uniformly distributed in metals. The initial velocities of hot carriers were assigned randomly and distributed isotropically. This can be achieved by setting the polar and azimuthal angles as $\theta = \pi\alpha_1$ and $\varphi = 2\pi\alpha_2$, separately, with α_i as independent random number between 0 and 1. To account for the scattering events, we calculated the scattering length for each hot carrier as $d_s = \xi\alpha_3$, where ξ is the mean free path. If d_s is larger than the distance between the hot carrier and the M/S interface, the hot carrier is taken as effective hot carrier that can be injected into the semi-

conductor. Then we chose three structures for the Au/TiO_2 and TiN/TiO_2 junctions: planar bilayer, planar sandwich trilayer, and core/shell cylinder, as depicted in Fig. 6. The sizes of the Au and TiN layers range from 5 nm to 100 nm. It should be pointed out that the Monte Carlo method provides an upper-bound for the estimation of η, because only the effect of Schottky barrier is considered for the reflection of hot carriers at the M/S interface, while the other factors existing in practical devices such as defects and lattice mismatch are neglected.

As shown in Fig. 6, the TiN/TiO_2 junction possesses much larger η than Au/TiO_2. This can be understood as follows. First, the band alignment between TiN and TiO_2 is better than that between Au and TiO_2, so the Fermi level of TiN is very close to the conduction band minimum of TiO_2. Second, the Schottky barrier at the TiN/TiO_2 interface is only 0.1eV, much smaller than that of the Au/TiO_2 interface. Third, TiN has much more effective hot electrons than Au as shown in Fig. 4. Therefore, TiN might be a promising plasmonic material to replace Au in practical hot-carrier devices.

It can be seen that η depends on the incident photon energy $h\nu$. For the Au/TiO_2 junction, the amplitude of η increases monotonically as $h\nu$ increases in the whole considered energy range. For the TiN/TiO_2 junction, the value of η increases rapidly when $h\nu$ increases from 0.1 eV to 0.6 eV and reaches the maximum value around 0.6 eV. As $h\nu$ further increases, η decreases monotonically, due to the increasing S_{ee} and S_{ep}. On the other hand, the thickness of the TiN layer has negative effect on η. At the same $h\nu$, η decreases as the thickness of TiN increases. In fact, this is evident because the lifetime and mean free path of the hot electrons are almost independent of the thickness. However, the thickness of the TiN layer cannot be too thin, because the number of hot electrons will be limited. Accordingly, the optimal thickness of the TiN layer should be smaller than but close to the

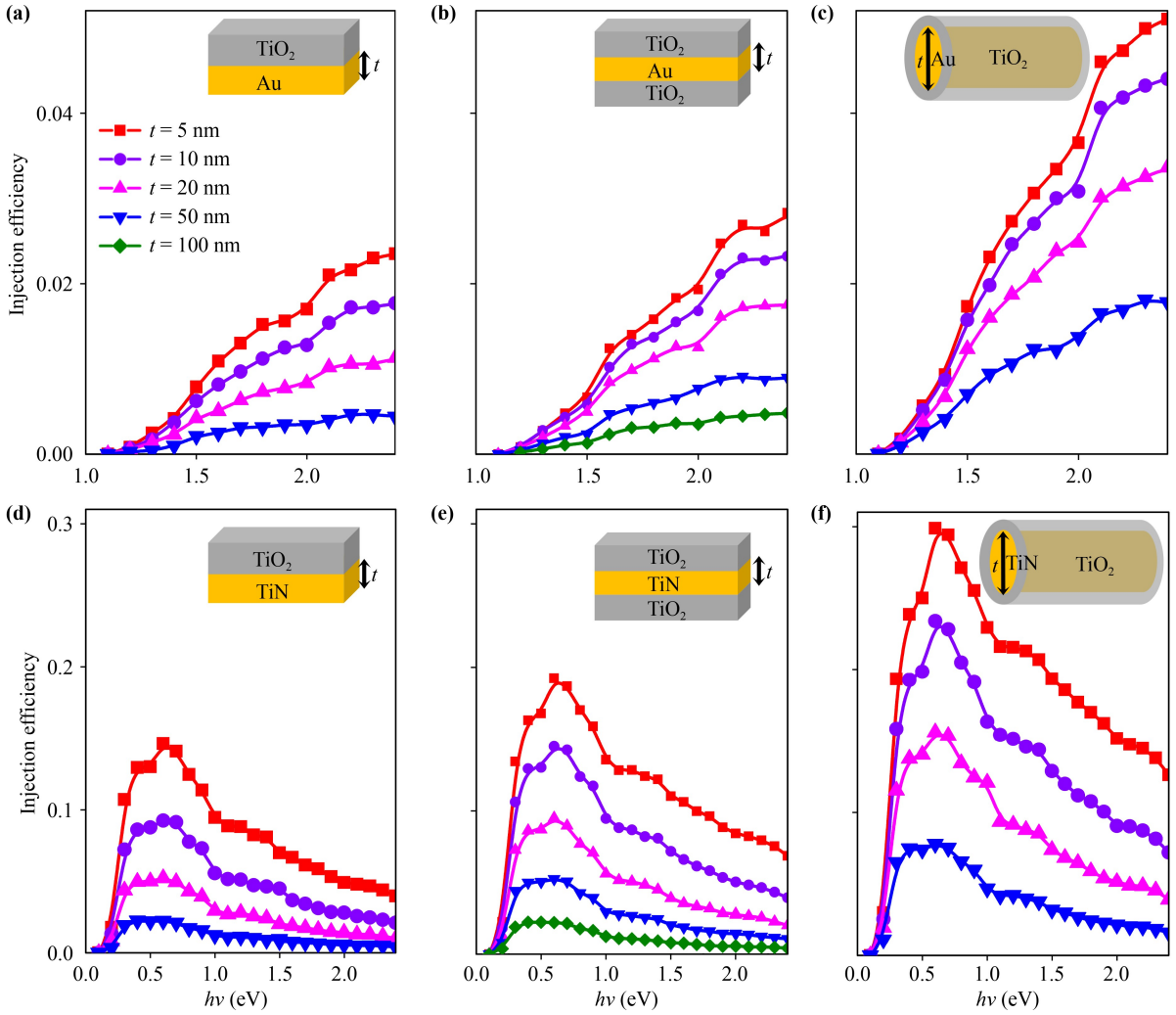

Fig. 6 Injection efficiency of hot electrons as a function of incident photon energy $h\nu$ in Au/TiO_2 and TiN/TiO_2 junctions. The insets depict the structures of the junctions: planar bilayer, planar sandwich trilayer, and core/shell cylinder. t denotes the thickness or diameter of Au and TiN.

mean free path of the hot electrons.

The structure of the junction also affects η, as seen in Fig. 6. First of all, η in the planar sandwich trilayer TiN/TiO_2 junction is nearly twice of that in the planar bilayer TiN/TiO_2 junction with the same thickness of TiN. Apparently, both TiO_2 layers in the former collect the hot electrons, if we assume that the hot electrons are distributed uniformly in TiN. The core/shell cylindrical TiN/TiO_2 junction can further enhance η, which can be understood as follows. In general, the distribution of the velocities of the hot electrons is almost isotropic in TiN, so that all hot electrons that reach the TiN/TiO_2 interface can be injected into the TiO_2 layer in the core/shell cylindrical TiN/TiO_2 junction. In contrast, the hot electrons with velocity parallel to the TiN/TiO_2 interface in the planar TiN/TiO_2 junctions will be lost. Therefore, the core/shell cylindrical junction is preferred in practical hot-carrier devices, and very large η is expected to be achieved.

4 Conclusions

In summary, we carried out first-principles calculations and Monte Carlo simulations to study the performance of the generation, transport and injection of hot carriers in the Au/TiO_2 and TiN/TiO_2 junctions. We found that TiN has much higher concentration of hot carriers in low energy range than Au, because of the high density of states around the Fermi level in TiN. The lifetime and mean free path of the hot carriers in TiN are comparable to those in Au, which benefits the hot-carrier transport. Interestingly, almost all hot electrons in TiN can be injected into TiO_2 as hot carriers, because of the specific band alignment and low Schottky barrier of ~ 0.1 eV of the TiN/TiO_2 junction. Compared to the Au/TiO_2 junction, the average energy of hot carriers in TiN/TiO_2 is much lower and the injection efficiency is much larger. The injection efficiency depends on the thickness of TiN, the structure of the junction and the incident photon energy. The optimal thickness of TiN should be close to the mean free path of the hot electrons, and the maximum injection efficiency is achieved in the core/shell cylindrical TiN/TiO_2 junction with the incident photon energy around 0.6 eV.

Acknowledgements We really appreciate the financial support from the National Natural Science Foundation of China (Grant Nos. 61875143, 61905170, 62075146, and 11574223), the Natural Science Foundation of Jiangsu Province (Nos. BK20180042, BK20181169, and BK20190816), the Natural Science Foundation of the Jiangsu Higher Education Institutions of China (No. 17KJA480004), the Priority Academic Program Development (PAPD) of Jiangsu Higher Education Institution, and the start-up funding of Ningbo University, and the Yongjiang Recruitment Project (No. 432200942).

Conflict of interest The authors have no conflicts to disclose.

Data availability The data that support the findings of this study are available from the corresponding author upon reasonable request.

References

1. C. Clavero, Plasmon-induced hot-electron generation at nanoparticle/metal–oxide interfaces for photovoltaic and photocatalytic devices, *Nat. Photonics* 8(2), 95 (2014)
2. M. W. Knight, H. Sobhani, P. Nordlander, and N. J. Halas, Photodetection with active optical antennas, *Science* 332(6030), 702 (2011)
3. Y. Tian and T. Tatsuma, Plasmon-induced photoelectrochemistry at metal nanoparticles supported on nanoporous TiO_2, *Chem. Commun.* 16(16), 1810 (2004)
4. C. Scales and P. Berini, Thin-film Schottky barrier photodetector models, *IEEE J. Quantum Electron.* 46(5), 633 (2010)
5. G. V. Naik, V. M. Shalaev, and A. Boltasseva, Alternative plasmonic materials: Beyond gold and silver, *Adv. Mater.* 25(24), 3264 (2013)
6. L. J. Krayer, K. J. Palm, C. Gong, A. Torres, C. E. P. Villegas, A. R. Rocha, M. S. Leite, and J. N. Munday, Enhanced near-infrared photoresponse from nanoscale Ag–Au alloyed films, *ACS Photonics* 7(7), 1689 (2020)
7. G. Tagliabue, J. S. DuChene, M. Abdellah, A. Habib, D. J. Gosztola, Y. Hattori, W. H. Cheng, K. Zheng, S. E. Canton, R. Sundararaman, J. Sá, and H. A. Atwater, Ultrafast hot-hole injection modifies hot-electron dynamics in Au/p–GaN heterostructures, *Nat. Mater.* 19(12), 1312 (2020)
8. M. Ortolani, A. Mancini, A. Budweg, D. Garoli, D. Brida, and F. de Angelis, Pump-probe spectroscopy study of ultrafast temperature dynamics in nanoporous gold, *Phys. Rev. B* 99(3), 035435 (2019)
9. Y. J. Chang and K. H. Shih, Solar energy conversion via internal photoemission in aluminum, copper, and silver: Band structure effects and theoretical efficiency estimates, *J. Appl. Phys.* 119(18), 183101 (2016)
10. A. J. Leenheer, P. Narang, N. S. Lewis, and H. A. Atwater, Solar energy conversion via hot electron internal photoemission in metallic nanostructures: Efficiency estimates, *J. Appl. Phys.* 115(13), 134301 (2014)
11. T. P. White and K. R. Catchpole, Plasmon-enhanced internal photoemission for photovoltaics: Theoretical efficiency limits, *Appl. Phys. Lett.* 101(7), 073905 (2012)
12. R. T. Ross and A. J. Nozik, Efficiency of hot-carrier solar energy converters, *J. Appl. Phys.* 53(5), 3813 (1982)
13. R. Sundararaman, P. Narang, A. S. Jermyn, W. A. III Goddard, and H. A. Atwater, Theoretical predictions for hot-carrier generation from surface plasmon decay, *Nat. Commun.* 5(1), 5788 (2014)
14. A. M. Brown, R. Sundararaman, P. Narang, W. A. III Goddard, and H. A. Atwater, Nonradiative plasmon decay and hot carrier dynamics: Effects of phonons, surfaces, and geometry, *ACS Nano* 10(1), 957 (2016)
15. F. Ladstädter, U. Hohenester, P. Puschnig, and C. Ambrosch-Draxl, First-principles calculation of hot-electron scattering in metals, *Phys. Rev. B* 70(23), 235125

(2004)
16. T. Gong and J. N. Munday, Materials for hot carrier plasmonics, *Opt. Mater. Express* 5(11), 2501 (2015)
17. D. Y. Lee, J. H. Park, Y. H. Kim, M. H. Lee, and N. I. Cho, Effect of Nb doping on morphology, crystal structure, optical band gap energy of TiO_2 thin films, *Curr. Appl. Phys.* 14(3), 421 (2014)
18. Q. Guo, C. Y. Zhou, Z. B. Ma, and X. M. Yang, Fundamentals of TiO_2 photocatalysis: Concepts, mechanisms, and challenges, *Adv. Mater.* 31(50), 1901997 (2019)
19. D. Z. Zhang, X. H. Gu, F. Y. Jing, F. L. Gao, J. G. Zhou, and S. B. Ruan, High performance ultraviolet detector based on TiO_2/ZnO heterojunction, *J. Alloys Compd.* 618, 551 (2015)
20. U. Bach, D. Lupo, P. Comte, J. E. Moser, F. Weissortel, J. Salbeck, H. Spreitzer, and M. Gratzel, Solid-state dye-sensitized mesoporous TiO_2 solar cells with high photon-to-electron conversion efficiencies, *Nature* 395(6702), 583 (1998)
21. E. Traver, R. A. Karaballi, Y. E. Monfared, H. Daurie, G. A. Gagnon, and M. Dasog, TiN, ZrN, and HfN nanoparticles on nanoporous Aluminum oxide membranes for solar-driven water evaporation and desalination, *ACS Appl. Nano Mater.* 3(3), 2787 (2020)
22. M. Kumar, N. Umezawa, S. Ishii, and T. Nagao, Examining the performance of refractory conductive ceramics as plasmonic materials: A theoretical approach, *ACS Photonics* 3(1), 43 (2016)
23. M. W. Yu, S. Ishii, S. L. Shinde, N. K. Tanjaya, K. P. Chen, and T. Nagao, Direct observation of photoinduced charge separation at transition-metal nitride–semiconductor interfaces, *ACS Appl. Mater. Interfaces* 12(50), 56562 (2020)
24. M. Marlo and V. Milman, Density-funcitional study of bulk and surface properties of titanium nitride using different exchange-correlation functional, *Phys. Rev. B* 62(4), 2899 (2000)
25. X. H. Chen, R. T. Pekarek, J. Gu, A. Zakutayev, K. E. Hurst, N. R. Neale, Y. Yang, and M. C. Beard, Transient evolution of the built-in field at junctions of GaAs, *ACS Appl. Mater. Interfaces* 12(36), 40339 (2020)
26. A. Naldoni, U. Guler, Z. X. Wang, M. Marelli, F. Malara, X. G. Meng, L. V. Besteiro, A. O. Govorov, A. V. Kildishev, A. Boltasseva, and V. M. Shalaev, Broadband hot-electron collection for solar water splitting with plasmonic titanium nitride, *Adv. Opt. Mater.* 5(15), 1601031 (2017)
27. U. Guler, A. Boltasseva, and V. M. Shalaev, Refractory plasmonics, *Science* 344(6181), 263 (2014)
28. G. V. Naik, J. L. Schroeder, X. J. Ni, A. V. Kildishev, T. D. Sands, and A. Boltasseva, Titanium nitride as a plasmonic material for visible and near-infrared wavelengths, *Opt. Mater. Express* 2(4), 478 (2012)
29. D. McIntyre, J. E. Greene, G. Hakansson, J. E. Sundgren, and W. D. Münz, Oxidation of metastable single-phase polycrystalline $Ti_{0.5}Al_{0.5}N$ films: Kinetics and mechanisms, *J. Appl. Phys.* 67(3), 1542 (1990)
30. P. Bordone, C. Jacoboni, P. Lugli, L. Reggiani, and P. Kocevar, Monte Carlo analysis of hot-phonon effects on non-polar semiconductor transport properties, *Physica B+C* 134(1−3), 169 (1985)
31. A. Piryatinski, C. K. Huang, and T. J. T. Kwan, Theory of electron transport and emission from a semiconductor nanotip, *J. Appl. Phys.* 125(21), 214301 (2019)
32. E. Blandre, D. Jalas, A. Y. Petrov, and M. Eich, Limit of efficiency of hot electrons in metals and their injection inside a semiconductor using a semiclassical approach, *ACS Photonics* 5(9), 3613 (2018)
33. G. Kresse and J. Furthmuller, Efficiency of *ab-initio* total energy calculations for metals and semiconductors using a plane-wave basis set, *Comput. Mater. Sci.* 6(1), 15 (1996)
34. G. Kresse and J. Furthmuller, Efficient iterative schemes for ab initio total-energy calculations using a plane-wave basis set, *Phys. Rev. B* 54(16), 11169 (1996)
35. G. Kresse and D. Joubert, From ultrasoft pseudopotentials to the projector augmented-wave method, *Phys. Rev. B* 59(3), 1758 (1999)
36. J. P. Perdew, A. Ruzsinszky, G. I. Csonka, O. A. Vydrov, G. E. Scuseria, L. A. Constantin, X. L. Zhou, and K. Burke, Restoring the density-gradient expansion for exchange in solids and surfaces, *Phys. Rev. Lett.* 100(13), 136406 (2008)
37. S. L. Dudarev, G. A. Botton, S. Y. Savrasov, C. J. Humphreys, and A. P. Sutton, Electron-energy-loss spectra and the structural stability of nickel oxide: An LSDA+U study, *Phys. Rev. B* 57(3), 1505 (1998)
38. A. Habib, F. Florio, and R. Sundararaman, Hot carrier dynamics in plasmonic transition metal nitrides, *J. Opt.* 20(6), 064001 (2018)
39. K. A. Mills, R. F. Davis, S. D. Kevan, G. Thornton, and D. A. Shirley, Angle-resolved photoemission determination of Λ-line valence bands in Pt and Au using synchrotron radiation, *Phys. Rev. B* 22(2), 581 (1980)
40. N. W. Ashcroft, N. D. Mermin, and W. Dan, Solid State Physics, revised edition, Cengage Leaning Asia PTe Ltd, 2016
41. D. Gall, I. Petrov, N. Hellgren, L. Hultman, J. E. Sundgren, and J. E. Greene, Growth of poly- and single-crystal ScN on MgO (001): Role of low-energy N^{2+} irradiation in determining texture, microstructure evolution, and mechanical properties, *J. Appl. Phys.* 84(11), 6034 (1998)
42. R. Sundararaman, K. Letchworth-Weaver, K. A. Schwarz, D. Gunceler, Y. Ozhabes, and T. A. Arias, JDFTx: Software for joint density-functional theory, *SoftwareX* 6, 278 (2017)
43. M. Schlipf and F. Gygi, Optimization algorithm for the generation of ONCV pseudopotentials, *Comput. Phys. Commun.* 196, 36 (2015)
44. N. Marzari and D. Vanderbilt, Maximally localized generalized Wannier functions for composite energy bands, *Phys. Rev. B* 56(20), 12847 (1997)
45. X. Xu, A. Dutta, J. Khurgin, A. Wei, W. M. Shalaev, and A. Boltasseva, TiN@TiO_2 core-shell nanoparticles as plasmon-enhanced photosensitizers: The role of hot electron injection, *Laser Photonics Rev.* 14(5), 1900376 (2020)
46. D. C. Ratchford, A. D. Dunkelberger, I. Vurgaftman, J. C. Owrutsky, and P. E. Pehrsson, Quantification of effi-

cient plasmonic hot-electron injection in gold nanoparticle-TiO_2 films, *Nano Lett.* 17(10), 6047 (2017)

47. G. Tagliabue, A. S. Jermyn, R. Sundararaman, A. J. Welch, J. S. Duchene, R. Pala, A. R. Davoyan, P. Narang, and H. A. Atwater, Quantifying the role of surface plasmon excitation and hot carrier transport in plasmonic devices, *Nat. Commun.* 9(1), 3394 (2018)
48. C. Zhang, K. Wu, V. Giannini, and X. F. Li, Planar hot-electron photodetection with Tamm plasmons, *ACS Nano* 11(2), 1719 (2017)
49. A. A. Mostofi, J. R. Yates, Y. S. Lee, I. Souza, D. Vanderbilt, and N. Marzari, Wannier90: A tool for obtaining maximally-localized Wannier functions, *Comput. Phys. Commun.* 178(9), 685 (2008)
50. N. Marzari, A. A. Mostofi, J. R. Yates, I. Souza, and D. Vanderbilt, Maximally localized Wannier functions: Theory and applications, *Rev. Mod. Phys.* 84(4), 1419 (2012)
51. D. Gerbert and P. Tegeder, Absorbate-mediated relaxation dynamics of hot electrons at metal/organic interfaces, *Phys. Rev. B* 96(14), 144304 (2017)
52. S. Stair, R. G. Johnston, and T. C. Bagg, Spectral distribution of energy from the sun, *J. Res. Natl. Bur. Stand.* 53(2), 113 (1954)
53. H. R. Condit and F. Grum, Spectral energy distribution of daylight, *J. Opt. Soc. Am.* 54(7), 937 (1964)